

Microstructural evolution, strengthening and thermal stability of an ultrafine-grained Al-Cu-Mg alloy

Ying Chen^{a,b}, Nong Gao^{b*}, Gang Sha^{c,d}, Simon P. Ringer^d, Marco J. Starink^b

^aMetal Materials, School of Materials Science and Engineering, Xiamen University of Technology, Xiamen 361024, China

^bMaterials Research Group, Faculty of Engineering and the Environment, University of Southampton, SO17 1BJ, UK

^c Herbert Gleiter Institute of Nanoscience, Nanjing University of Science and Technology, Nanjing 210094, China

^dARC Centre of Excellence for Design in Light Metals, School of Aerospace, Mechanical & Mechatronic Engineering, Australian Centre for Microscopy & Microanalysis, The University of Sydney, NSW 2006, Australia

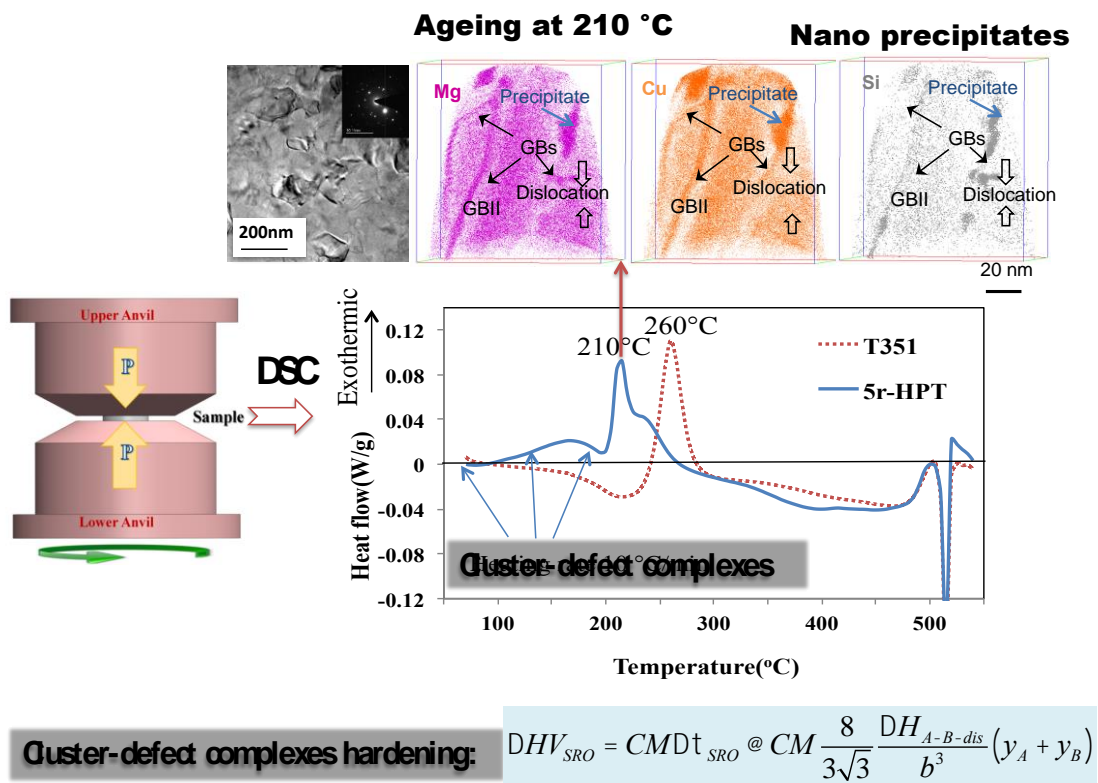
Abstract

To gain insight into the origin of the ultra-high strength of ultrafine-grained (UFG) alloys, the solute clustering, precipitation phenomena, and microstructural evolutions were studied in an UFG Al-4.63Cu-1.51Mg (wt.%) alloy (AA2024) processed by high-pressure torsion (HPT). The thermal analysis was performed using differential scanning calorimetry. The microstructures, internal microstrains and hardness following heating at a constant rate were characterised at room temperature using X-ray diffraction (XRD), transmission electron microscopy (TEM) and atom probe tomography (APT). The microhardness of the HPT processed sample initially increases following heating to 140 °C, and then remains unchanged on further heating to 210°C. As the temperature increases up to 210 °C, the crystallite size calculated from XRD line broadening remains about 60~70 nm, while the dislocation densities remain in excess of $2 \times 10^{14} \text{ m}^{-2}$. A multimechanistic model is established to describe the strengthening due to grain refinement, dislocation accumulation, solid

solution, precipitation, solute clusters and their segregation. The analysis reveals that solute clusters and lattice defects are key factors in HPT-induced strengthening of alloys, and illustrates the interactions between alloying elements, dislocations and grain boundaries enhance strength and stabilize ultrafine microstructures. Furthermore, for an HPT sample heated beyond 210 °C, the formation of nano-precipitates also contributes to hardness increment. The multimechanistic model for hardness contribution indicates the short-range order strengthening due to cluster-defect complexes is the dominant mechanism, which accounts for more than 40% of overall hardness.

Keywords: Al-Cu-Mg alloy; High-pressure torsion; Differential scanning calorimetry; Strengthening mechanism; Atom-probe tomography

Graphical Abstract



1. Introduction

Severe plastic deformation (SPD) methods have attracted wide attentions as effective techniques to improve the mechanical properties of metals and alloys without changing their overall dimensions [1]. The high-pressure torsion (HPT) process has advantages over other SPD techniques due to its high efficiency in inducing a large density of dislocations and its good capability for continuous deformation. Over 20 years of research in HPT has demonstrated that the hardness and the strength of materials increase and often evolve to saturation with large straining [2-4].

A number of strengthening models have been developed to incorporate work hardening and grain refinement hardening [5-11]. A model predicting dislocation generation due to non-shearable particles was first proposed by Ashby [5]. The concept of dislocations generated and annihilated in grain boundaries then was incorporated in the models developed by Estrin and Mecking [7, 11] and further refinements [7, 8]. Further modified models have been applied to predict strength of SPD-processed aluminum and its alloys [9, 10]. However, in these strengthening models, the alloying atom effects have not received much attention. The study by Edalati et al. [12] indicates that the solute atoms lead to extra grain refinement, causing an extra increase in strength. Recent advances in atom probe tomography (APT) have revealed solute atoms significantly segregate to grain boundaries in 7xxx and 6xxx Al alloys [13-15] and some pre-existing precipitates are fragmented or partially dissolved in Al-Cu alloys [16-20]. In their studies on Al alloys [13-20], the increase of hardness can be partially attributed to the solute segregation and precipitate fragmentation.

In a precipitation-strengthening Al-Cu-Mg alloy, nanosized Cu-Mg clusters and/or uniformly dispersed precipitates are presented within the Al matrix after ageing heat treatment [21-23]. The investigation indicates both Cu-Mg clusters and S-phase contribute to overall strengthening in Al-Cu-Mg alloy during the heat treatment

processes [24]. A specific question comes out - what will be the solute clusters and dispersed precipitates behavior in heating processes, if the samples contain a large number of dislocations. Obviously, a large amount of energy is stored in the lattice defects as dislocations accumulate to grain boundaries and the grains become ultrafine [25-28]. At the same time, alloying elements are able to reduce the grain-boundary energy and enhance the thermal stability of nanostructured alloys [13, 29, 30]. It is essential to develop a deep understanding of the mechanisms that govern the redistribution of solute clusters, precipitates and dislocations.

More recently, the studies on the precise determination of the underlying strengthening mechanisms for precipitation-strengthening Al alloys processed by SPD were discussed [31-33]. It was suggested that the dramatic increase of strength after SPD process was attributed to the multiple mechanisms which comprised strengthening due to grain boundaries, dislocations, solid solution and precipitates [31, 32]. However, most of recent predictions do not consider the co-cluster effects in the origin stage of HPT-processed Al-Cu-Mg alloys. Our recent studies [33] indicate the defect-cluster complexes are formed in ternary Al alloys when the number of dislocations and vacancies reach its saturation after HPT processes. The defect-cluster complexes are thermally stable and contribute to a primary part in strengthening. It is of great importance to formulate a quantitative insight into strengthening mechanisms, providing a direct guide of the microstructural modifications for industrial heat treatment.

The previous analysis [34-37] on small Cu-Mg clusters and dispersed precipitates were trying to reveal the essence of the strength increase in the heat-treated Al-Cu-Mg alloys. To the best of our knowledge, the quantitative predictions of strengthening at an increasing temperature have not been reported for UFG Al-Cu-Mg alloys, and this is the first time to address the multiple strengthening mechanisms that comprised cluster-defect complexes strengthening. The aim of this work is to investigate solute redistribution, evolution of dislocation density and nanoscale precipitation during

linear heating of HPT-processed AA2024 alloy, mainly using APT and X-ray diffraction line broadening.

2. Experimental procedures

UFG Al-4.63Cu-1.51Mg (*wt. %*) (AA2024) samples were processed by HPT for five revolutions (5r-HPT) at room temperature, under a pressure of 6 GPa with a speed of 1 rpm. The composition of the alloy is shown in Table 1, and the as-received specimens were in the T351 temper. Prior to HPT, the samples were cut to discs with a diameter of 9.8 mm and mechanically ground and polished to 0.83~0.85 mm in thickness. Details of the HPT processing were explained previously [9, 38].

Thermal analysis was performed using a differential scanning calorimeter (Perkin-Elmer DSC1) at heating rate of 10 °C/min in a flowing N₂ atmosphere from ambient temperature to 540 °C. The samples were put in copper pans under tight-fitted inverted lids, with an empty copper pan as the reference. Prior to DSC experiments, the near disk shaped samples were punched from the HPT disk at 4 mm from the centre using a 5 mm diameter punch. Each sample is approximately 20 mg. The DSC thermograms were corrected by subtracting a baseline run with an empty copper pan and a further baseline correction as described in [39] was applied.

Additionally, HPT processed discs were heated and held at temperature T_{iso} in a furnace. The hold time was chosen such that the heat treatment is equivalent to heating at the DSC heating rate, β , to the final temperature, T_f . The equivalent time t_{eq} of an isothermal heat treatment at T_{iso} has been approximated by using the theory for thermally activated reactions [39], which provides:

$$t_{eq} @ 0.786T_f/b(RT_f/E)^{0.95} \exp(-E/RT_f) \exp(-E/RT_{iso})^{-1} \quad \text{Eq.1}$$

where E is the activation energy of the reaction, taken as 107 kJ/mole [40]. Thus, the HPT samples were heat treated for the calculated equivalent time t_{eq} at the same temperature in the DSC curve ($T_{iso}=T_f$), *e.g.* a sample isothermal annealed at 210 °C for 2 minutes equivalent to that DSC linear heated up to 210 °C with a constant

heating rate, 10 °C/min. These equivalent heat treatments were applied on the samples for hardness, XRD, TEM and APT tests.

Vickers hardness was measured on T351 and 5r-HPT processed samples after heating to selected temperatures in the range 100 to 400°C and with holding times to produce the equivalent treatment ($T_{iso}=T_f$) defined by Eq. 1, followed by rapid cooling (cooling rate ~ 50 K/min). The hardness tests were conducted at room temperature immediately after completion of the cooling. Each sample was prepared by grinding to 4000-grid SiC paper and polishing to a mirror-like surface. The hardness tests were conducted using a load of 500 g for a dwell time of 15 s. Each reported value is the mean of 6 indentations all made at a distance of 4 mm from the centre of the disc.

XRD was carried out using a Siemens D5000 diffractometer equipped with a graphite monochromator using Cu $K\alpha$ radiation at 50 steps per degree and a count time of 1s per step. The Maud software [41-43] was used to analyse the microstrains and the crystallite sizes of HPT-processed samples and those under isothermal heat treatment. The analysis of XRD peak broadening is based on the full peak X-ray profile refinement (Rietveld method) [42, 44, 45].

TEM was performed on HPT-processed samples and heat-treated samples using a JEOL 3100 TEM operated at 300 kV. The samples were first ground to ~150 μm in thickness, and disc shaped samples of 3 mm in diameter were punched out at about 4 mm from the centre of a disk. Subsequently, the samples were thinned to perforation using twin-jet electropolishing at -30 °C with an electrolyte solution of HNO₃: methanol=1:3 (in volume). The statistic average grain sizes were obtained based on 20 TEM images. Selected area diffraction (SAD) patterns were taken with an aperture of ~1 μm^2 .

APT specimens in the form of sharp needles with an end radius of less than 100 nm were prepared from blanks with dimensions of 0.5 × 0.5 × 10 mm³ using a standard two-stage electro polishing technique. The first stage used a solution of 25% perchloric acid in acetic acid at 15 V, whereas the second stage used an electrolyte of 5% perchloric acid in 2-butoxyethanol at 20 V. APT analysis was carried out under an

ultrahigh vacuum ($\sim 1 \times 10^{-8}$ Pa), UV laser pulsing energy of 40 pJ at the pulse repetition rate of 200 kHz and a specimen temperature of ~ 20 -25 K using a local electrode atom probe (LEAP4000X SI®). Reconstruction and visualization of APT data was performed using the Imago Visualization and Analysis Software (IVAS™ 3.6.2) [22]. The maximum separation algorithm was employed for cluster identification, with Mg, Si and Cu as clustering solutes and a separation distance of 0.5 nm [22, 23]. The cluster sizes represent the number of solute atoms in the detected clusters. A minimum cluster size of $n = 2$ was employed to detect extremely small solute clusters [22].

3. Results and Analysis

3.1 The DSC and Vickers hardness measurements

In Fig. 1, the DSC thermogram of the T351 sample has an endothermic reaction at 100~240 °C, whilst 5r-HPT sample shows an exothermic reaction with peak at 170 °C. In the intermediate temperature range, the T351 sample shows a single exothermic peak at 260 °C, whilst the 5r-HPT shows two overlapping exothermic effects, peaking respectively at 210 °C and 240 °C. These exothermic effects are primarily due to the formation of variants of the S phase [46]. The high temperature endotherm (from about 270 °C to 490 °C) is mainly due to the dissolution of S precipitates. A significant amount of stored energy is released as microstructures evolve on heating. The microhardness evolution of samples heated at a constant heating rate of 10 °C/min is shown in Fig. 2. The microhardness increases significantly after HPT process: the microhardness of the HPT sample is ~70% higher than that of T351 (142 HV). On heating, the microhardness of the HPT-processed sample increases slightly from 243 HV to 263 HV when heated to 140 °C, where exhibits an exothermic peak in DSC (Fig. 1). The microhardness of the 5r-HPT sample decreases significantly when heated beyond 210 °C; and the decrease in microhardness for the T351 sample occurs from temperature above 260 °C. Both samples have similar microhardness when heated between 300 °C and 400 °C.

3.2 Microstructural characterisation

3.2.1 XRD analysis

The XRD patterns of 5r-HPT samples heated to different temperatures are shown in Fig. 3. The appearance of peaks due to S (Al_2CuMg) precipitates in the samples annealed up to 240 °C and 300 °C evidences the precipitation reaction. The differences of relative peak intensities indicate HPT processing changes the textures of the alloy. The broadening of the aluminium XRD profile of HPT-processed samples is due to lattice defects, which are predominantly dislocations and (additional) grain boundaries. In cubic crystals, anisotropic peak broadening may occur due to anisotropic crystallite shape, anisotropic strain or planar defects, which are caused by dislocations, stacking faults, twinning and stress gradients [47, 48]. Crystal twinning does not normally occur in aluminium alloys due to their high stacking fault energy, and compared to other metals, *i.e.* Cu or Ni, anisotropy effects are small in aluminium alloys. Hence for the present samples anisotropic peak broadening is assumed to be negligible.

3.2.2 Microstructural evolution during equivalent isothermal annealing

Through Rietveld refinement [42, 44, 45], the microstrain and crystallite size are optimized simultaneously by whole profile fitting on the XRD data, and the results are shown in Fig. 4(a). The microstrain of the 5r-HPT sample increase from about 0.0018 at room temperature to 0.0021 after heating to 120 °C. This small increase can be due to cluster formation, which are detected by APT (see below) and corresponds to the first small exothermic peak in DSC thermogram (Fig. 1). A significant decrease of microstrain was observed after heating beyond 120 °C. The value of microstrain approaches 0.0007 at 300 °C, which is close to the as-obtained T351 sample (0.0009) at room temperature. The crystallite size of samples heating to temperatures below 210 °C is about constant at around 60 to 70 nm, while it increases significantly to 310 nm after heating to 300 °C. This combination of reduced microstrain and increased

crystallite size are the key factors contributing to the hardness decrease in the corresponding temperature range. The dislocation density ρ was calculated from the measured microstrain $\langle \varepsilon^2 \rangle^{1/2}$ by [26, 49]:

$$r = \frac{2\sqrt{3}\langle \varepsilon^2 \rangle^{1/2}}{D_c b} \quad \text{Eq. 2}$$

where b is the Burgers vector, 0.286 nm, for an fcc Al alloy, D_c is the crystallite size. Fig. 4(b) illustrates the dislocation density evolution of the 5r-HPT samples heated to various temperatures.

The average grain size of the 5r-HPT samples was determined from TEM images, shown in Fig. 5, using the modified line intercept method described in [9]. The grain size d was taken as $d=1.455\bar{L}$, where \bar{L} is the average line intercept [50]. The average grain size of 5r-HPT sample is 157 ± 30 nm ($\bar{L}=108$ nm), and it is virtually unchanged at 169 ± 30 nm ($\bar{L}=116$ nm) on heating to 210 °C (5r-HPT-210 °C), and increases to 250 ± 40 nm on heating to 300 °C (5r-HPT-300 °C). The SAD pattern in the 5r-HPT sample, shown in Fig. 5(a), indicates the presence of many grains, compared with the 5r-HPT-210 °C and the 5r-HPT-300 °C samples (Fig. 5(b) and (c)). The grain size of SPD-processed materials determined by TEM is several times larger than the crystallite size (or coherently scattering domain size) obtained by X-ray peak profile analysis [51, 52].

3.2.3 Solute segregation and clustering

The 5r-HPT sample and the samples subsequently subjected to equivalent annealing have been analysed by APT. The cluster number density (CND, the number of clusters per unit volume) of different types of clusters and their fractions of number density to overall clusters obtained by APT are shown in Table 2.

Linear profile analysis across GBs in Fig. 6 and Fig. 7 has been conducted; a typical one is shown in Fig. 7b. The solute concentrations at the GB are significantly higher than those values in the matrix of two grains on either side of the GB, confirming that there is segregation of solutes at the grain boundary. All grain boundaries were

identified due to their 2-D curved plane features by carefully visual examination of the analysis volume in different view directions.

The solute-enriched features in the volume element of the 5r-HPT sample (Fig. 6) involve: (i) a segment of grain boundary; (ii) a uniform distribution of fine scale solute-rich clusters (containing up to 50 solute atoms) with a number density of $1.99 \times 10^{26} \text{ m}^{-3}$ (as determined from the total number of solute clusters identified in the analysed volume). The vast majority of the segregants are Cu, and a small but a significant minor concentration of Si and Mn is also evident in the corresponding atoms maps. The segregation of Mg atoms is not so obvious as other atoms, because Mg atoms are absent in Mn-rich particles and more homogeneously distributed within the grains.

Fig. 7 shows Mg, Cu and Si atom maps of an analysed volume of a 5r-HPT sample heated to 210 °C. This volume contains three grain boundaries and some small precipitates. It illustrates a similar solute enrichment of Mg, Cu and Si as those of grain boundary segments in Fig. 7(a), while dislocations with Cu and Mg atoms segregated on them are observed at the right bottom of each map. The total number density of solute clusters in this volume is identified as $1.11 \times 10^{26} \text{ m}^{-3}$. The number density of Mg-Cu co-clusters decreases significantly from $1.06 \times 10^{26} \text{ m}^{-3}$ after HPT processing to $0.60 \times 10^{26} \text{ m}^{-3}$ after subsequent heating to 210 °C. Fig. 7(b) illustrates the concentrations of Mg, Cu and Si with its z-axis parallel to the plane normal of the grain boundary (GB) II in Fig. 7(a). It indicates the ratio of Cu and Mg at GBII is close to 1, but the concentration of Mg is higher than that of Cu as the distance is in the range of 5 nm to 15 nm from grain boundaries, with 0.3 at% as the maximum imbalance.

The APT analysis of the 5r-HPT-300 °C sample in Fig. 8 shows Cu and Mg rich in a precipitate as well as a thin grain boundary line in the lower right of the figure. The measured composition of the coarse particle indicates a ratio of Al:Cu:Mg equalling 2:1:1, and considering the XRD results (Fig. 3) this precipitate is identified as S phase (Al_2MgCu). On heating, the total cluster number density decreases significantly to

$2.42 \times 10^{25} \text{ m}^{-3}$, while the density of Cu-Mg co-clusters, which is the majority of the clusters, decreases to $1.22 \times 10^{25} \text{ m}^{-3}$.

APT work on a solution treated and aged 2024 Al alloy shows that solute clusters form during ageing by aggregation of the main alloying elements Cu and Mg, along with the minor elements Si and Zn [23]. In the HPT-deformed samples, the clustering phenomenon is similar [33]. The main alloy elements Mg and Cu concentrate along the grain boundaries or dislocation walls together with minor element Si. The size of the nano-precipitates increases as the annealing temperature increases.

4. Discussion

4.1 A multimechanistic model for hardening

The current study demonstrates the hardness changes of an Al-Cu-Mg alloy due to HPT processing and ageing post-HPT are caused by a range of factors including solute clustering, defect-solute clustering, dislocation creation and subsequent annihilation, grain refinement and precipitation. In this Section we will analyse the multiple strengthening mechanisms that affect the hardness using models that were introduced recently [10, 33, 38, 53]. The main goal of this analysis is to highlight the dominant strengthening mechanisms for UFG Al-Cu-Mg alloys during heating and provides an explanation of UFG structural stability at elevated temperatures. To improve clarity we will here simplify the hardness-strength relation and consider that for our samples the relation between Vickers hardness and yield strength can be approximated through $HV = C\sigma$, where in good approximation C is a constant [10, 33, 53-57], and we will not consider the potential effect of crystallographic texture. The value of C for worked Al alloys ranges from 3.06 to 3.28 [55, 56], and here the average value 3.16 is adopted [10].

The yield strength of a polycrystalline alloy is related to the critically resolved shear stress (CRSS) of the grain and grain boundary strengthening. As a result, the total hardness increase, ΔHV_{total} , is due to dislocation hardening ΔHV_d , grain boundary hardening ΔHV_{gb} , solid solute hardening ΔHV_{ss} and cluster hardening which includes

both short-range order hardening, ΔHV_{SRO} [58, 59] and modulus hardening, ΔHV_m [60, 61]. For samples aged after HPT, hardening due to precipitation, ΔHV_p , needs to be considered, as S/S' precipitates are present (see XRD patterns in Fig. 3 and in APT data in Fig. 7 and Fig. 8). Therefore the sample hardness can be approximated as:

$$HV = HV_0 + DHV_d + DHV_{gb} + DHV_{ss} + DHV_{SRO} + DHV_m + DHV_p \quad \text{Eq.3}$$

where HV_0 is the hardness of annealed Al, which is very low (i.e. ~20 HV for high purity Al 99.99% [62]). To account for the small amount of Mn, Fe and Si present in our alloy, the HV_0 is taken as 30 HV [10, 63, 64]. Predictions of the contributions of each hardening mechanism for an UFG Al-Cu-Mg alloy are described below.

Dislocation hardening

Dislocations mutually interact hindering their motion. The increase of dislocation density thus leads to an increment of hardness, which is given by (see e.g. [31, 33, 63, 65]):

$$DHV_d = CM\alpha_1 Gb\sqrt{r_{total}} \quad \text{Eq. 4}$$

where α_1 is a constant taken as 0.3 [33], M is the mean orientation factor, usually termed the Taylor factor and taken as 2.6 [9, 10, 66, 67], G is the shear modulus of the alloy and b is the Burgers vector [31, 33, 63, 65]. In our study, the dislocation densities ρ_{total} due to the contribution of cell boundaries (identified as crystallite size in Section 3.2.2) and microstrains are calculated using XRD full profile refinement. The values of the parameters in the Eq. 4 and subsequent equations, which are all taken from either the literature or the analysis presented in Section 3, are summarized in Table 3.

Grain boundary hardening

The hardness due to grain boundary strengthening is taken according to the Hall-Petch relationship [68-70], i.e. the hardness increment due to grain boundaries is taken as proportional to $d^{-1/2}$ [71]:

$$DHV_{gb} = Ck_{HP}/d^{1/2} \quad \text{Eq. 5}$$

where k_{HP} is the Hall-Petch constant, and d is the grain size [65]. Recent experimental work has indicated k_{HP} is within the range of 0.06-0.09 MPa/m^{-1/2} for a nanostructured Al-Cu alloy [72]; whilst a theoretical assessment has indicated $k_{HP} = 0.062$ MPa/m^{-1/2} [65]. We adopt the latter value. The dislocation and continuum mechanics models [70] indicate grain size strengthening of metals can be driven by constraints on stress and dislocation curvature. The hardening effects by dislocations or grain boundaries are correlated with each other; essentially, they are driven by the disorder atom arrangement in lattice.

Solute hardening

Solid solution strengthening depends on the concentration of solute atoms dissolved in the Al matrix as [34, 64]:

$$DHV_{ss} = CM \sum k_j c_j^n \quad \text{Eq. 6}$$

where k_j are factors related to the strengthening due to the individual elements and c_j are the concentration of the alloying elements in solid solution [34, 73, 74]. n is a constant, taken as 1 [34, 64]. In the present alloy processed by HPT, solid solution strengthening has a relatively small contribution to overall strength, accounting for up to 4% to overall strength. Whilst the Eq. 6 may be a good approximation for coarse grained alloys, this relationship cannot fully predict the solute atom effects for fine grained alloys as solute atoms segregate to grain boundaries (see Fig. 6), which provides an additional strengthening effect [75]. In our UFG ternary Al-Cu-Mg alloy, the Cu and Mg atoms form nanometer-sized solute clusters at selected grain boundaries/junctions. Their contribution to strength will be calculated and discussed in the following sections.

Cluster hardening and cluster-defect complexes hardening

The co-existence of cluster-dislocation complexes and the intragranular solute clusters contributes to the extra strengthening in UFG Al-Cu-Mg alloys [33]. These solute clusters are very small (typically less than a nm) and consist typically of Cu and Mg

[13, 23, 33, 76, 77].

The strengthening due to co-clusters is related to the obstacle shearing [58, 59]. A single dislocation passing through clusters causes a disruption of the local short-range order (SRO) and hence causes changes in lattice energy. The increase of critical resolved shear stress due to the clusters given as [78]:

$$D t_{SRO} = g_{SRO}/b \quad \text{Eq. 7}$$

where γ_{SRO} is the change in energy per unit area on slip planes on passing of one dislocation, which is related to the enthalpy of the nearest neighbor bonding ΔH_{A-B} and the change in area density of A–B nearest neighbour bonds crossing the slip plane on the passage of one dislocation, i.e. $\rho_{A-B (n=0)} - \rho_{A-B (n=1)}$ [58, 59].

A-B clusters associated with vacancies along grain boundaries and dislocations possess a changed bonding energy, denoted as $\Delta H_{A-B-dis}$. The description and illustration of clusters segregated structures has been presented in Ref [33], providing

$$D t_{SRO} @ \frac{DH_{A-B-dis}}{b} \frac{4}{\sqrt{3}b^2} \frac{2}{3} (y_A + y_B) \quad \text{Eq. 8}$$

where $\Delta H_{A-B-dis}$ is the average enthalpy of the various types of A-B-dislocation clusters at the dislocations, y_A and y_B are the amount of A and B atoms in the co-clusters, respectively. Thus, the hardness increment due to cluster SRO strengthening is given as

$$DHV_{SRO} = CMD t_{SRO} @ CM \frac{8}{3\sqrt{3}} \frac{DH_{A-B-dis}}{b^3} (y_A + y_B) \quad \text{Eq. 9}$$

The average enthalpy $\Delta H_{A-B-dis}$ depends on the fractions of each type of atoms and clusters segregated at the grain boundaries and dislocations, and the intragranular clusters:

$$DH_{A-B-dis} = f_1 DH_{A-B} + f_2 DH_{A-dis} + f_3 DH_{B-dis} + f_4 DH_{(A-B)_n-dis} \quad \text{Eq. 10}$$

where f_1 to f_4 are the fraction of A-B intragranular clusters, and atoms A, B or A-B clusters segregated to dislocations and grain boundaries. ΔH_{A-B} is the enthalpy of A-B co-clusters in M matrix, ΔH_{A-dis} , ΔH_{B-dis} the enthalpy of single atom A or B located at dislocations, $\Delta H_{(A-B)_n-dis}$ the enthalpy of co-clusters located at dislocations. $\Delta H_{Cu-Mg-dis}$ has been determined as 50 ± 5 kJ/mole in samples deformed by HPT up to the hardness

saturation level, when shear strain is larger than 500% [33].

The modulus difference between particle zones (clusters, GPB zones) and the Al matrix leads to an interaction force [60]. It is this force that contributes to a further increment of hardness related to co-clusters. The hardening due to the difference in shear modulus is presented as follow [61]:

$$\Delta HV_m = CM \frac{\Delta\mu}{4\rho\sqrt{2}} \sqrt{f_{cl}} \quad \text{Eq. 11}$$

where $\Delta\mu$ is difference in shear modulus between particles and Al matrix. This approximation has been adopted in a range of works [34, 37, 58, 61], and the f_{cl} is the average fraction of Cu-Mg clusters in Al-Cu-Mg alloy, as volume of other types of clusters are very small. The hardening due to modulus difference for the present samples is calculated to be only 14~15% of the short-range order hardening, i.e. it is relatively close to the result from Ref [79].

Precipitate hardening

At a temperature higher than 210 °C, the amount of clusters in the HPT-processed Al-Cu-Mg samples reduces as they transform into S/S' phases. S/S' precipitates are considered to be non-shearable and the hardness increment is approximated using the Orowan bypassing mechanism as [37]

$$\Delta HV_p = CM \frac{0.81\mu_m b}{2\rho(1-\nu)^{1/2}} \ln\left(\frac{d_s}{b}\right) \left(0.615d_s \sqrt{\frac{2\rho}{3f_s}} - d_s\right)^{-1} \quad \text{Eq. 12}$$

where μ_m is the shear modulus of the matrix, ν the Poisson's ratio for Al, d_s is the diameter of the cross-section of the S-phase precipitates and f_s is the volume fraction of S phase [37], which is determined in the Appendix. The diameter of the cross-section of S precipitates were determined from APT data as 10 nm and 50 nm for 5r-HPT sample annealed at 210 °C and 300 °C.

4.2 The superposition of multiple strengthening mechanisms

The results of the present assessment of the strengthening mechanisms are presented

in Table 4. The table shows a good correspondence between measured and predicted total hardness, which further supports the present model. Thus the present approach provides a coherent explanation of the hardness of the present complex SPD processed alloy on the conditions both after HPT and after subsequent heating, revealing the relative importance of the various strengthening mechanisms. In particular, the model shows that for samples where the maximum exposure temperature is 210°C or lower, the solute/cluster-defect complex hardening is the dominant mechanism, contributing an increase of ~100 HV, over 40% of the total strength.

A key element in the approach relates to the interaction enthalpy of the Cu-Mg-defect complexes. The magnitude of enthalpy for a dislocation cutting through a short-range ordered structure strongly depends on the fractions (i.e. f_1 to f_4 in Eq. 10) of different types of atoms and clusters segregated at dislocations or grain boundaries. Eq. 9 and Eq. 10 are valid for any types of co-clusters including two-atom clusters and four-atom clusters [33]. In Eq. 10, the fractions of f_1 to f_4 change as the temperature increases in the DSC heating process. As indicated in [58, 59], f_1 in Eq. 10 accounts for all clusters in the Al-rich phase for a T351 sample; as a result, the $\Delta H_{A-B-dis}$ is approximated as the value of ΔH_{Cu-Mg} , which is 34.5 kJ/mole [58] in Cu-Mg clusters. However, for samples processed by HPT to near the saturation level in hardness, substantial cluster-defect complexes form and enthalpy for a dislocation passing through Cu-Mg-defect clusters increases to 50 kJ/mole [33]. The $\Delta H_{Cu-Mg-dis}$ may vary somewhat during heating, as the dislocation density slightly decreases (see Fig. 4(b)) and part of the Cu-Mg clusters dissolve into the Al matrix.

The microstrain increases on heating to 120 °C as shown in Fig. 4(a). This is due to the interaction between dislocations and dissolved Cu/Mg atoms, when dislocations pass through and break down Cu-Mg clusters to smaller clusters. As a result of increasing atom diffusion coefficient for a UFG Al alloy in DSC heating process, more clusters are segregated to grain boundaries, and then the proportion f_4 of cluster-defect complexes increases.

Finally it is noted that the mechanism of strengthening in nanostructured Al alloys discussed by Valiev et al [75, 80] indicates the effect of solute segregation on the emission of dislocations from the grain boundaries results in an additional strengthening and a positive deviation of Hall-Petch slope k_{HP} , which is 0.13 MPa/m^{1/2}. It shows a good agreement with the Hall-Petch coefficient in Al-Cu [72] and Al-Mg-Si alloys [81]. This may be interpreted as an indication that in the alloys studied in those works the solute-grain boundary interaction is the dominant solute-defect strengthening effect. Whilst these works [75, 80] on an experimental formula between grain size and strength is valuable, a modified Hall-Petch slope in itself does not clarify the nanoscale mechanisms responsible for the strengthening effects. The analysis in the present work shows a clear evidence that the nanoscale mechanisms play a role in a ternary alloy.

5. Conclusions

The hardness, clusters/nanoscale precipitates and dislocations in an UFG Al-4.3Cu-1.51Mg alloy processed by HPT and subsequently heated were investigated using XRD, TEM, APT and DSC. The contributions from different hardening mechanisms were quantitatively calculated. Conclusions are drawn as follows:

1. The UFG Al-Cu-Mg alloy processed by 5r-HPT presents a much higher hardness (~100 HV) than the conventionally processed T351 sample. The hardness of the UFG Al-Cu-Mg alloy is stable, only starting to decrease during heating beyond 210 °C.
2. The dislocation densities and the grain size are stable during heating up to 210 °C, the solute clusters segregate to the UFG grain boundaries and dislocations. As a result of precipitation, the cluster-defect complexes disappear as heated beyond 210 °C.
3. The analysis of contributions of hardness indicates short-range order due to the cluster-defect complexes is the dominant mechanism, contributing to ~100 HV for samples heated up to 210 °C. The hardness due to the microstrains related to defects in lattice (i.e. dislocation and grain boundaries) contributes the second hardening component (totaling ~90 HV). Solute hardening and modulus hardening contribute

very little. A precipitation-hardening component from Orowan bypass mechanism occurs due to S phase formation.

Appendix: Volume fraction of S phase

The volume fraction of a precipitate is related to the atomic fraction, following [82]:

$$f_v = \frac{x\Omega^p}{x\Omega^p + (1-x)\Omega^m} \quad \text{Eq. A.1}$$

where Ω^p and Ω^m are atomic volumes of precipitates and matrix, and x is atomic fraction of precipitates. In 2024 Al alloy, the S precipitate has a Cmc_m structure with the lattice parameters $a=0.400$ nm, $b=0.923$ nm and $c=0.714$ nm and $\Omega^p=26.36 \times 10^{-3}$ nm⁻³ [36], containing 24 atoms per unit cell. The atom number of S phase is triple times of Al unit cell, as a result, $\Omega^m = 3(a_{Al})^3 = 26.38 \times 10^{-3}$ nm⁻³. In this case, the Eq. A.1 simplifies as $f_v=x$.

The volume fraction of precipitates varies during the DSC heat treatment [63]. At particular temperature T , the fraction of precipitates forms is given by:

$$f_0 = f_{\max} \frac{c_s - c_0}{c_s} \quad \text{Eq. A.2}$$

where f_{\max} is maximum value that f_0 can take, i.e. when all elements would precipitate. Thus the maximum volume fraction of S phase f_{\max} is equal to the fraction of Cu-Mg co-clusters, which is 0.018. c_s is the composition of the alloy, c_0 is the equilibrium concentration and expressed as [63].

$$c_0 = c_s \exp\left\{-\frac{Q_s}{R} \left(\frac{1}{T} - \frac{1}{T_s}\right)\right\} \quad \text{Eq. A.3}$$

where Q_s is the free energy of solution, R is the gas constant, T_s is the solvus temperature. For a phase $M_mA_aB_bC_c$, the best approximation of Q_s is $\Delta H_{sol}/(a+b+c)$ [63], thus Q_s is taken as $\Delta H_{Mg-Cu}/2$. In the computed vertical section of Al-4.5Cu- (x_{Mg}) Mg (wt.%) alloy phase diagram [83], the S phase precipitates at 260 °C if x_{Mg} is 1.5wt.%. It is consistent with the DSC thermogram of a 2024 Al-T351 sample in Fig. 1. This analysis suggests that T_s equals 260 °C.

Acknowledgements

One of the authors (Y. Chen) gratefully acknowledges China Scholarship Council for a Ph.D scholarship to study in University of Southampton, and thanks to High-level Personnel of Special Support Program from Xiamen University of Technology (No. YKJ15025R) for a grant in aid of continuous research.

Table captions

Table 1 Composition (wt.%) of the Al-Cu-Mg alloy studied.

Table 2 The experimental cluster number density (CND) of Cu-Cu, Mg-Mg and Cu-Mg type clusters and their fractions in overall clusters number density

Table 3 Parameters used in the strengthening mechanism calculations.

Table 4 Hardness increments for the different strengthening mechanisms obtained from the models in Section 4.1.

Figure captions

Fig. 1 DSC curves for Al-4.63Cu-1.51Mg T351 and 5r-HPT samples.

Fig. 2 Vickers hardness of T351 and the 5r-HPT samples equivalent annealed up to varying temperatures with a heating rate of 10 °C/min.

Fig. 3 XRD patterns of T351 and the 5r-HPT samples equivalent annealed up to varying temperatures with a heating rate of 10 °C/min. The diffraction plane indices of aluminum are indicated in the figures.

Fig. 4 (a) Microstrain and crystallite size and (b) dislocation density evolution of 5r-HPT samples equivalent annealed up to varying temperatures with a heating rate of 10 °C/min.

Fig. 5 TEM bright field images of 5r-HPT samples in (a) as HPT processed condition, (b) after heating to 210 °C, and (c) after heating to 300 °C. The corresponding selected area diffraction patterns are at the top-right corner.

Fig. 6 Mg, Cu, Si and Mn atom maps of 5r-HPT sample aged at ambient temperature near Mn-rich particles.

Fig. 7 APM of 5r-HPT sample annealed at 210 °C (a) Mg, Cu and Si atom maps (b) Mg, Cu and Si profiles measured using an analysis box with its z-axis parallel to the plane normal of the grain boundary.

Fig. 8 (a) Mg, Cu and Si atom maps of 5r-HPT sample aged at 300°C (b) concentration profiles of Al, Mg, and Si across the precipitates (the balance is Cu).

Reference

- [1] A.P. Zhilyaev, T.G. Langdon. Using high-pressure torsion for metal processing: Fundamentals and applications, *Progress in Materials Science* 53 (2008) 893-979.
- [2] R.Z. Valiev, R.K. Islamgaliev, I.V. Alexandrov. Bulk nanostructured materials from severe plastic deformation, *Progress in Materials Science* 45 (2000) 103-189.
- [3] Y. Estrin, A. Vinogradov. Extreme grain refinement by severe plastic deformation: A wealth of challenging science, *Acta Materialia* 61 (2013) 782-817.
- [4] R.K.W. Marceau, C. Qiu, S.P. Ringer, C.R. Hutchinson. A study of the composition dependence of the rapid hardening phenomenon in Al–Cu–Mg alloys using diffusion couples, *Materials Science and Engineering: A* 546 (2012) 153-161.
- [5] M.F. Ashby. The deformation of plastically non-homogeneous materials, *Philosophical Magazine* 21 (1970) 399 - 424.
- [6] N. Hansen. The effect of grain size and strain on the tensile flow stress of aluminium at room temperature, *Acta Metallurgica* 25 (1977) 863-869.
- [7] Y. Estrin. Dislocation theory based constitutive modelling: foundations and applications, *Journal of Materials Processing Technology* 80-81 (1998) 33-39.
- [8] Y. Estrin, A. Molotnikov, C.H.J. Davies, R. Lapovok. Strain gradient plasticity modelling of high-pressure torsion, *Journal of the Mechanics and Physics of Solids* 56 (2008) 1186-1202.
- [9] M.J. Starink, X.G. Qiao, J. Zhang, N. Gao. Predicting grain refinement by cold severe plastic deformation in alloys using volume averaged dislocation generation, *Acta Materialia* 57 (2009) 5796-5811.
- [10] X.G. Qiao, N. Gao, M.J. Starink. A model of grain refinement and strengthening of Al alloys due to cold severe plastic deformation, *Philosophical Magazine* 92 (2011) 446-470.
- [11] Y. Estrin, H. Mecking. A unified phenomenological description of work hardening and creep based on one-parameter models, *Acta Metallurgica* 32 (1984) 57-70.
- [12] K. Edalati, D. Akama, A. Nishio, S. Lee, Y. Yonenaga, J.M. Cubero-Sesin, Z. Horita. Influence of dislocation–solute atom interactions and stacking fault energy on grain size of single-phase alloys after severe plastic deformation using high-pressure torsion, *Acta Materialia* 69 (2014) 68-77.
- [13] P.V. Liddicoat, X.-Z. Liao, Y. Zhao, Y. Zhu, M.Y. Murashkin, E.J. Lavernia, R.Z. Valiev, S.P. Ringer. Nanostructural hierarchy increases the strength of aluminium alloys, *Nature Communications* 1 (2010) 63.
- [14] G. Nurislamova, X. Sauvage, M. Murashkin, R. Islamgaliev, R. Valiev. Nanostructure and related mechanical properties of an Al–Mg–Si alloy processed by severe plastic deformation, *Philosophical Magazine Letters* 88 (2008) 459-466.
- [15] G. Sha, L. Yao, X. Liao, S.P. Ringer, Z. Chao Duan, T.G. Langdon. Segregation of solute elements at grain boundaries in an ultrafine grained Al–Zn–Mg–Cu alloy, *Ultramicroscopy* 111 (2011) 500-505.
- [16] Z. Liu, X. Chen, X. Han, Y. Gu. The dissolution behavior of θ' phase in Al – Cu binary alloy during equal channel angular pressing and multi-axial compression, *Materials Science and Engineering: A* 527 (2010) 4300-4305.

- [17] Z. Liu, S. Bai, X. Zhou, Y. Gu. On strain-induced dissolution of θ' and θ particles in Al – Cu binary alloy during equal channel angular pressing, *Materials Science and Engineering: A* 528 (2011) 2217-2222.
- [18] W. Huang, Z. Liu, M. Lin, X. Zhou, L. Zhao, A. Ning, S. Zeng. Reprecipitation behavior in Al – Cu binary alloy after severe plastic deformation-induced dissolution of θ' particles, *Materials Science and Engineering: A* 546 (2012) 26-33.
- [19] M. Murayama, Z. Horita, K. Hono. Microstructure of two-phase Al–1.7 at% Cu alloy deformed by equal-channel angular pressing, *Acta Materialia* 49 (2001) 21-29.
- [20] W. Lechner, W. Puff, B. Mingler, M.J. Zehetbauer, R. Würschum. Microstructure and vacancy-type defects in high-pressure torsion deformed Al–Cu–Mg–Mn alloy, *Scripta Materialia* 61 (2009) 383-386.
- [21] R.K.W. Marceau, G. Sha, R. Ferragut, A. Dupasquier, S.P. Ringer. Solute clustering in Al–Cu–Mg alloys during the early stages of elevated temperature ageing, *Acta Materialia* 58 (2010) 4923-4939.
- [22] R.K.W. Marceau, G. Sha, R.N. Lumley, S.P. Ringer. Evolution of solute clustering in Al–Cu–Mg alloys during secondary ageing, *Acta Materialia* 58 (2010) 1795-1805.
- [23] G. Sha, R.K.W. Marceau, X. Gao, B.C. Muddle, S.P. Ringer. Nanostructure of aluminium alloy 2024: Segregation, clustering and precipitation processes, *Acta Materialia* 59 (2011) 1659-1670.
- [24] T.S. Parel, S.C. Wang, M.J. Starink. Hardening of an Al–Cu–Mg alloy containing Types I and II S phase precipitates, *Materials & Design* 31, Supplement 1 (2010) S2-S5.
- [25] H. Jiang, Y.T. Zhu, D.P. Butt, I.V. Alexandrov, T.C. Lowe. Microstructural evolution, microhardness and thermal stability of HPT-processed Cu, *Materials Science and Engineering A* 290 (2000) 128-138.
- [26] Y.H. Zhao, X.Z. Liao, Z. Jin, R.Z. Valiev, Y.T. Zhu. Microstructures and mechanical properties of ultrafine grained 7075 Al alloy processed by ECAP and their evolutions during annealing, *Acta Materialia* 52 (2004) 4589-4599.
- [27] B. Straumal, R. Valiev, O. Kogtenkova, P. Zieba, T. Czepe, E. Bielanska, M. Faryna. Thermal evolution and grain boundary phase transformations in severely deformed nanograined Al–Zn alloys, *Acta Materialia* 56 (2008) 6123-6131.
- [28] S.S. Hazra, A.A. Gazder, E.V. Pereloma. Stored energy of a severely deformed interstitial free steel, *Materials Science and Engineering: A* 524 (2009) 158-167.
- [29] T. Chookajorn, H.A. Murdoch, C.A. Schuh. Design of Stable Nanocrystalline Alloys, *Science* 337 (2012) 951-954.
- [30] R. Kirchheim. Grain coarsening inhibited by solute segregation, *Acta Materialia* 50 (2002) 413-419.
- [31] K. Ma, H. Wen, T. Hu, T.D. Topping, D. Isheim, D.N. Seidman, E.J. Lavernia, J.M. Schoenung. Mechanical behavior and strengthening mechanisms in ultrafine grain precipitation-strengthened aluminum alloy, *Acta Materialia* 62 (2014) 141-155.
- [32] I.F. Mohamed, Y. Yonenaga, S. Lee, K. Edalati, Z. Horita. Age hardening and thermal stability of Al–Cu alloy processed by high-pressure torsion, *Materials Science and Engineering: A* 627 (2015) 111-118.
- [33] Y. Chen, N. Gao, G. Sha, S.P. Ringer, M.J. Starink. Strengthening of an Al–Cu–Mg alloy processed by high-pressure torsion due to clusters, defects and defect–cluster complexes, *Materials Science and Engineering: A* 627 (2015) 10-20.
- [34] M.J. Starink, N. Gao, L. Davin, J. Yan, A. Cerezo. Room temperature precipitation in quenched Al–Cu–Mg alloys: a model for the reaction kinetics and yield strength development, *Philosophical Magazine* 85 (2005) 1395-1417.
- [35] M.J. Starink, N. Gao, J.L. Yan. The origins of room temperature hardening of Al–Cu–Mg alloys, *Materials Science and Engineering A* 387-389 (2004) 222-226.
- [36] S.C. Wang, M.J. Starink. Precipitates and intermetallic phases in precipitation hardening Al–Cu–Mg–(Li) based alloys, *International Materials Reviews* 50 (2005) 193-215.
- [37] S.C. Wang, F. Lefebvre, J.L. Yan, I. Sinclair, M.J. Starink. VPPA welds of Al-2024 alloys: Analysis and modelling of local microstructure and strength, *Materials Science and Engineering: A* 431 (2006) 123-136.
- [38] J. Zhang, N. Gao, M.J. Starink. Microstructure development and hardening during high pressure torsion of commercially pure aluminium: Strain reversal experiments and a dislocation based model, *Materials Science and Engineering: A* 528 (2011) 2581-2591.
- [39] M.J. Starink. Analysis of aluminium based alloys by calorimetry: quantitative analysis of reactions and reaction kinetics, *International Materials Reviews* 49 (2004) 191-226.

- [40] M.J. Starink, P.J. Gregson. A quantitative interpretation of DSC experiments on quenched and aged SiCp reinforced 8090 alloys, *Scripta Metallurgica et Materialia* 33 (1995) 893-900.
- [41] M. Ferrari, L. Lutterotti. Method for the simultaneous determination of anisotropic residual stresses and texture by X-ray diffraction, *Journal of Applied Physics* 76 (1994) 7246-7255.
- [42] L. Lutterotti, S. Gialanella. X-ray diffraction characterization of heavily deformed metallic specimens, *Acta Materialia* 46 (1998) 101-110.
- [43] L. Lutterotti, S. Matthies, H. Wenk. MAUD (material analysis using diffraction): a user friendly Java program for Rietveld texture analysis and more. *Proceeding of the Twelfth International Conference on Textures of Materials (ICOTOM-12)*, vol. 1: NRC Press Ottawa, Canada, 1999. p.1599.
- [44] H.M. Rietveld. A profile refinement method for nuclear and magnetic structure, *Journal of Applied Crystallography* 2 (1969) 67-71.
- [45] L.B. McCusker, R.B. Von Dreele, D.E. Cox, D. Louer, P. Scardi. Rietveld refinement guidelines, *Journal of Applied Crystallography* 32 (1999) 36-50.
- [46] S.C. Wang, M.J. Starink. Two types of S phase precipitates in Al-Cu-Mg alloys, *Acta Materialia* 55 (2007) 933-941.
- [47] T. Ungár. Microstructural parameters from X-ray diffraction peak broadening, *Scripta Materialia* 51 (2004) 777-781.
- [48] T. Ungár, J. Gubicza. Nanocrystalline materials studied by powder diffraction line profile analysis, *Zeitschrift fur Kristallographie* 222 (2007) 114-128.
- [49] G.K. Williamson, R.E. Smallman. III. Dislocation densities in some annealed and cold-worked metals from measurements on the X-ray debye-scherrer spectrum, *Philosophical Magazine* 1 (1956) 34-46.
- [50] A. Thorvaldsen. The intercept method—1. Evaluation of grain shape, *Acta Materialia* 45 (1997) 587-594.
- [51] J. Gubicza, I. Schiller, N.Q. Chinh, J. Illy, Z. Horita, T.G. Langdon. The effect of severe plastic deformation on precipitation in supersaturated Al-Zn-Mg alloys, *Materials Science and Engineering: A* 460-461 (2007) 77-85.
- [52] J. Gubicza, N.Q. Chinh, Z. Horita, T.G. Langdon. Effect of Mg addition on microstructure and mechanical properties of aluminum, *Materials Science and Engineering: A* 387-389 (2004) 55-59.
- [53] J. Zhang, N. Gao, M.J. Starink. Al-Mg-Cu based alloys and pure Al processed by high pressure torsion: The influence of alloying additions on strengthening, *Materials Science and Engineering: A* 527 (2010) 3472-3479.
- [54] M.A. Meyers, A. Mishra, D.J. Benson. Mechanical properties of nanocrystalline materials, *Progress in Materials Science* 51 (2006) 427-556.
- [55] X.G. Qiao, M.J. Starink, N. Gao. Hardness inhomogeneity and local strengthening mechanisms of an Al1050 aluminium alloy after one pass of equal channel angular pressing, *Materials Science and Engineering: A* 513-514 (2009) 52-58.
- [56] X.G. Qiao, M.J. Starink, N. Gao. The influence of indenter tip rounding on the indentation size effect, *Acta Materialia* 58 (2010) 3690-3700.
- [57] P. Zhang, S.X. Li, Z.F. Zhang. General relationship between strength and hardness, *Materials Science and Engineering: A* 529 (2011) 62-73.
- [58] M.J. Starink, S.C. Wang. The thermodynamics of and strengthening due to co-clusters: General theory and application to the case of Al-Cu-Mg alloys, *Acta Materialia* 57 (2009) 2376-2389.
- [59] M.J. Starink, L.F. Cao, P.A. Rometsch. A model for the thermodynamics of and strengthening due to co-clusters in Al-Mg-Si-based alloys, *Acta Materialia* 60 (2012) 4194-4207.
- [60] E. Nembach. Precipitation hardening caused by a difference in shear modulus between particle and matrix, *physica status solidi (a)* 78 (1983) 571-581.
- [61] P. Gomiero, Y. Brechet, F. Louchet, A. Tourabi, B. Wack. Microstructure and mechanical properties of a 2091 AlLi alloy--II. Mechanical properties: Yield stress and work hardening, *Acta Metallurgica et Materialia* 40 (1992) 857-861.
- [62] M. Kawasaki, R.B. Figueiredo, T.G. Langdon. An investigation of hardness homogeneity throughout disks processed by high-pressure torsion, *Acta Materialia* 59 (2011) 308-316.
- [63] M.J. Starink, S.C. Wang. A model for the yield strength of overaged Al-Zn-Mg-Cu alloys, *Acta Materialia* 51 (2003) 5131-5150.
- [64] S.C. Wang, Z. Zhu, M.J. Starink. Estimation of dislocation densities in cold rolled Al-Mg-Cu-Mn alloys by combination of yield strength data, EBSD and strength models, *Journal of Microscopy* 217 (2005) 174-178.
- [65] M.J. Starink, X. Cheng, S. Yang. Hardening of pure metals by high-pressure torsion: A physically based model employing volume-averaged defect evolutions, *Acta Materialia* 61 (2013) 183-192.

- [66] G.I. Taylor. The Mechanism of Plastic Deformation of Crystals. Part I. Theoretical, Proceedings of the Royal Society of London. Series A, Containing Papers of a Mathematical and Physical Character 145 (1934) 362-387.
- [67] G.I. Taylor. The Mechanism of Plastic Deformation of Crystals. Part II. Comparison with Observations, Proceedings of the Royal Society of London. Series A, Containing Papers of a Mathematical and Physical Character 145 (1934) 388-404.
- [68] E.O. Hall. The Deformation and Ageing of Mild Steel: III Discussion of Results, Proceedings of the Physical Society. Section B 64 (1951) 747.
- [69] N.J. Petch. The Cleavage Strength of Polycrystals, J. Iron Steel Inst. 174 (1953) 25-28.
- [70] R. Armstrong. Engineering science aspects of the Hall–Petch relation, Acta Mech 225 (2014) 1013-1028.
- [71] N. Hansen. Hall–Petch relation and boundary strengthening, Scripta Materialia 51 (2004) 801-806.
- [72] T. Shanmugasundaram, M. Heilmaier, B.S. Murty, V.S. Sarma. On the Hall–Petch relationship in a nanostructured Al–Cu alloy, Materials Science and Engineering: A 527 (2010) 7821-7825.
- [73] H.R. Shercliff, M.F. Ashby. A process model for age hardening of aluminium alloys—I. The model, Acta Metallurgica et Materialia 38 (1990) 1789-1802.
- [74] Ø. Ryen, B. Holmedal, O. Nijs, E. Nes, E. Sjölander, H.-E. Ekström. Strengthening mechanisms in solid solution aluminum alloys, Metallurgical and Materials Transactions A 37 (2006) 1999-2006.
- [75] R.Z. Valiev, N.A. Enikeev, M.Y. Murashkin, S.E. Aleksandrov, R.V. Goldshtein. Superstrength of ultrafine-grained aluminum alloys produced by severe plastic deformation, Dokl. Phys. 55 (2010) 267-270.
- [76] G. Sha, H. Möller, W.E. Stumpf, J.H. Xia, G. Govender, S.P. Ringer. Solute nanostructures and their strengthening effects in Al–7Si–0.6Mg alloy F357, Acta Materialia 60 (2012) 692-701.
- [77] G. Sha, K. Tugcu, X.Z. Liao, P.W. Trimby, M.Y. Murashkin, R.Z. Valiev, S.P. Ringer. Strength, grain refinement and solute nanostructures of an Al–Mg–Si alloy (AA6060) processed by high-pressure torsion, Acta Materialia 63 (2014) 169-179.
- [78] P.A. Flinn. Solute hardening of close-packed solid solutions, Acta Metallurgica 6 (1958) 631-635.
- [79] M. Liu, S. Bai, Z. Liu, X. Zhou, P. Xia, S. Zeng. Analysis of modulus hardening in an artificial aged Al–Cu–Mg alloy by atom probe tomography, Materials Science and Engineering: A 629 (2015) 23-28.
- [80] R.Z. Valiev, N.A. Enikeev, M.Y. Murashkin, V.U. Kazykhanov, X. Sauvage. On the origin of the extremely high strength of ultrafine-grained Al alloys produced by severe plastic deformation, Scripta Materialia 63 (2010) 949-952.
- [81] A. Loucif, R.B. Figueiredo, T. Baudin, F. Brisset, R. Chemam, T.G. Langdon. Ultrafine grains and the Hall–Petch relationship in an Al–Mg–Si alloy processed by high-pressure torsion, Materials Science and Engineering: A 532 (2012) 139-145.
- [82] A. Deschamps, A. Bigot, F. Livet, P. Auger, Y. Bréchet, D. Blavette. A comparative study of precipitate composition and volume fraction in an Al–Zn–Mg alloy using tomographic atom probe and small-angle X-ray scattering, Philosophical Magazine A 81 (2001) 2391-2414.
- [83] V. Raghavan. Al-Cu-Mg (Aluminum-Copper-Magnesium), J Phs Eqil and Diff 28 (2007) 174-179.

Tables

Table 1 Composition (wt.%) of the Al-Cu-Mg alloy studied

Cu	Fe	Mg	Mn	Si	Zn	Total others	Al
4.63	0.15	1.51	0.66	0.08	0.05	<0.05	balance

Table 2 The experimental cluster number density (CND) of Cu-Cu, Mg-Mg and Cu-Mg type clusters and their fractions in overall clusters number density

	Cluster type	Size (atoms)	CND $\times 10^{26}/\text{m}^3$	Fractions
5r-HPT	Cu-Cu	2-6	0.36	0.18
	Mg-Mg	2-8	0.45	0.23
	Cu-Mg	2-24	1.07	0.53
	Si -containing all		Balance 1.99	Balance
5r-HPT-210 °C	Cu-Cu	2-6	0.20	0.18
	Mg-Mg	2-8	0.26	0.23
	Cu-Mg	2-37	0.6	0.54
	Si -containing all		Balance 1.11	Balance
5r-HPT-300 °C	Cu-Cu	2-6	0.04	0.18
	Mg-Mg	2-8	0.07	0.29
	Cu-Mg	2-34	0.12	0.50
	Si -containing all		Balance 0.24	Balance

Table 3 Parameters used in the strengthening mechanism calculations.

Mechanisms	Symbol	Value	References
	C	3.16	[55, 56]
	M	2.6	[9, 10, 66, 67]
	b	0.286 nm	[31, 33, 63, 65]
	G/μ_m	27 GPa	[31, 33, 63, 65]
Dislocation hardening	α_1	0.3	[31, 33, 63, 65]
	ρ	This work	Taken from the XRD fitting

Grain-boundary hardening	k_{HP}	0.062 MPa*m ^{-1/2}	[65]
	d	This work	Taken from TEM
Solute hardening	k_{Cu}	10.5 MPa/at% Cu	[34, 73, 74]
	k_{Mg}	5 MPa/at% Mg	[34, 73, 74]
	n	1	[34, 64]
Short-range order phase/Cluster-defect complexes hardening	$\Delta H_{A-B-dis}$	50±5 kJ/mole	[33]
Modulus hardening	f_{cl}	This work	0.018 as the maximum
	$\Delta\mu$	3.4 GPa	[33]
Precipitation hardening	ν	0.3	[37]
	d_s	This work	Taken from the APT
	f_{max}	0.018	[82]

Table 4 Hardness increments for the different strengthening mechanisms obtained from the models in Section 4.1.

	5r-HPT	5r-HPT-210°C	5r-HPT-300°C
ΔHV_d	35.2±1	29.5±0.5	10.2±0.3
ΔHV_{gb}	51±5	49.5±4.5	40±3
ΔHV_{ss}	5.1	5.1	5.5
ΔHV_{SRO}	107±11	107±11	—
ΔHV_m	15.7	15.0	15.2
ΔHV_p	—	21.7	20.2
HV_0	30	30	30
$HV_{predict}$	245±12	258±12	121±3
$HV_{measured}$	244±4	256±9	134±7

Figures

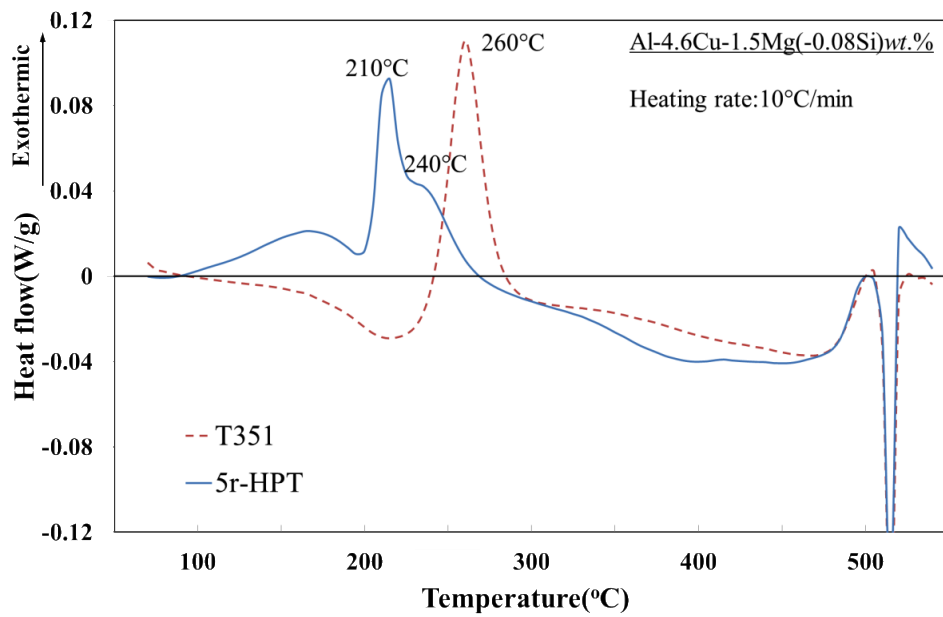


Fig. 1 DSC curves for Al-4.63Cu-1.51Mg T351 and 5r-HPT samples.

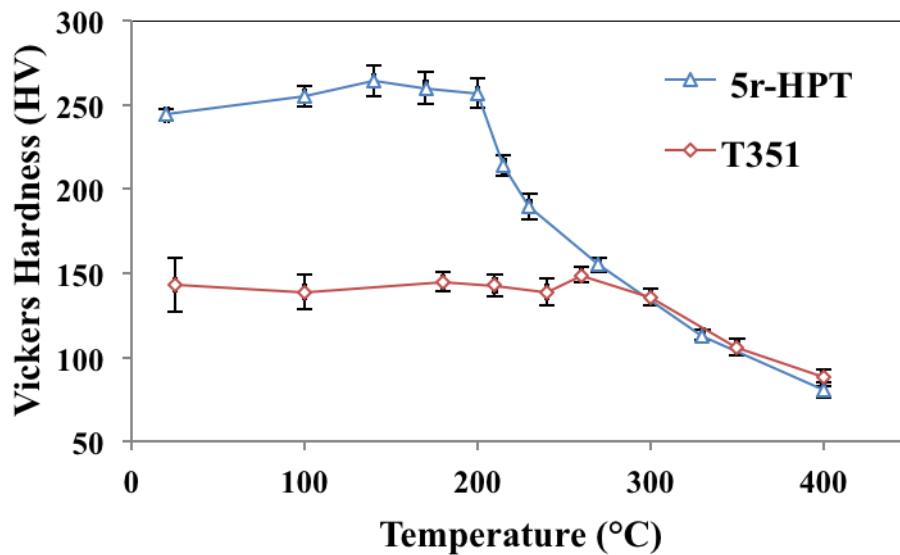


Fig. 2 Vickers hardness of T351 and the 5r-HPT samples equivalent annealed up to varying temperatures with a heating rate of 10 °C/min.

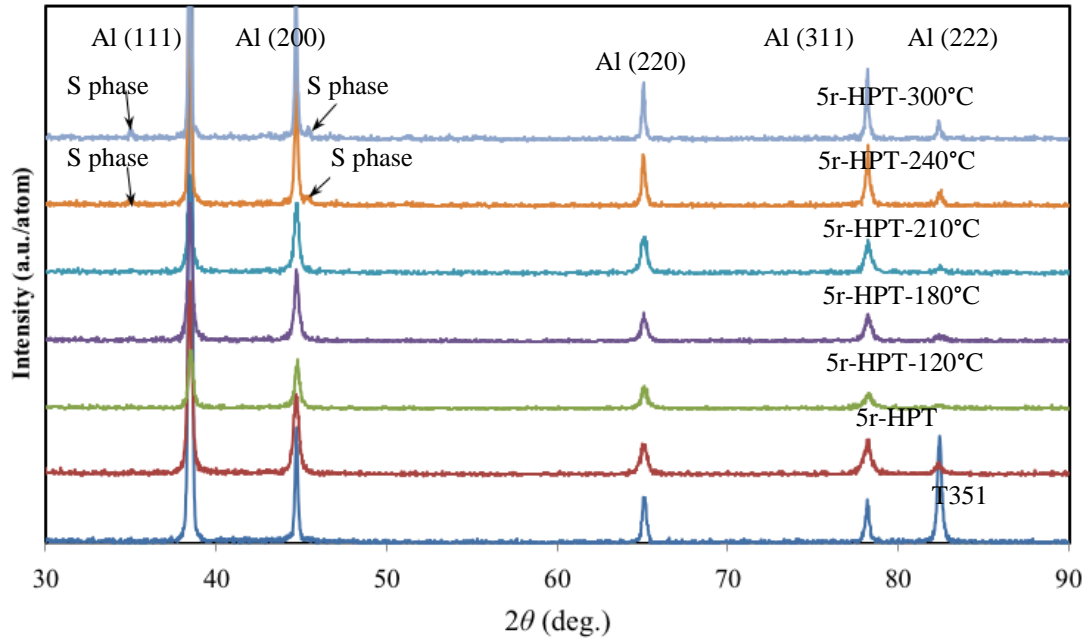


Fig. 3 XRD patterns of T351 and the 5r-HPT samples equivalent annealed up to varying temperatures with a heating rate of 10 °C/min. The diffraction plane indices of aluminum are indicated in the figures.

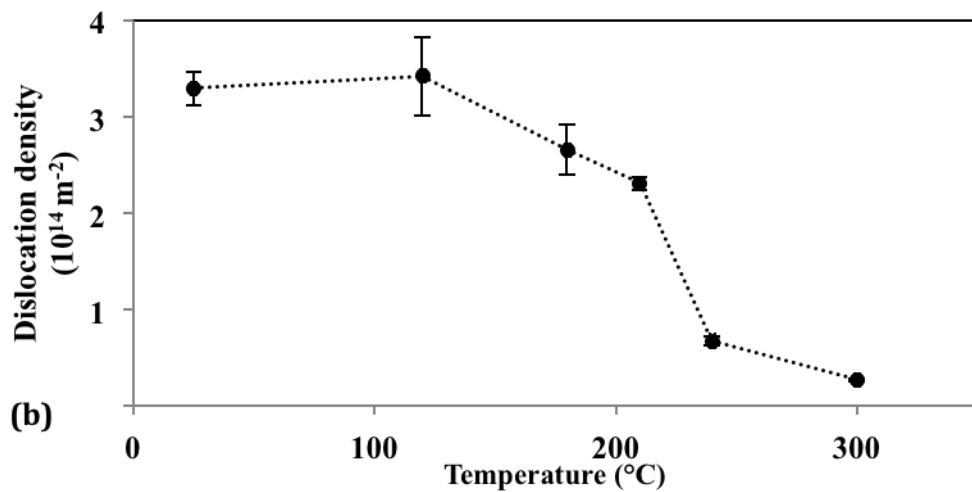
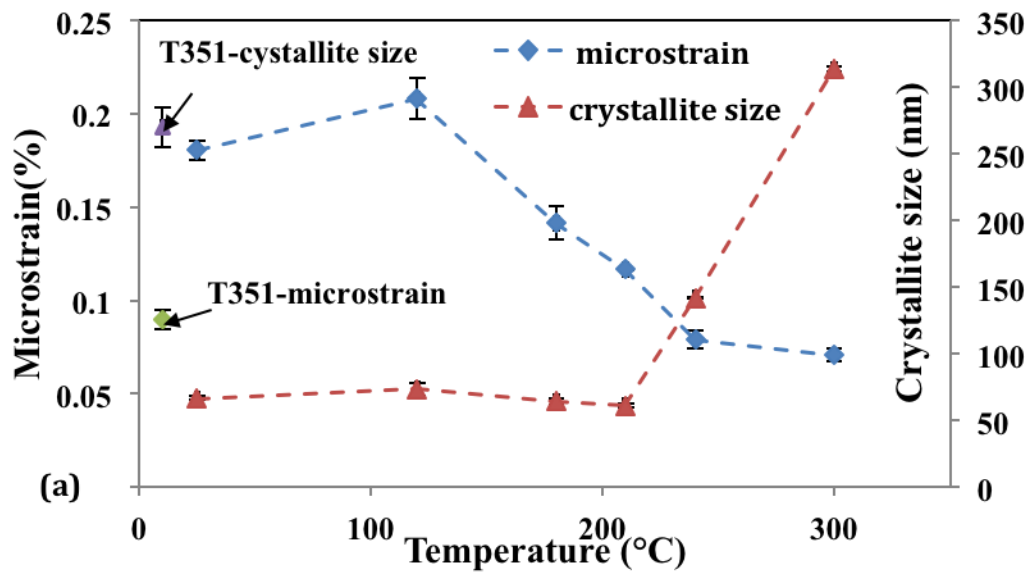


Fig. 4 (a) Microstrain and crystallite size and (b) dislocation density evolution of 5r-HPT samples equivalent annealed up to varying temperatures with a heating rate of 10 °C/min.

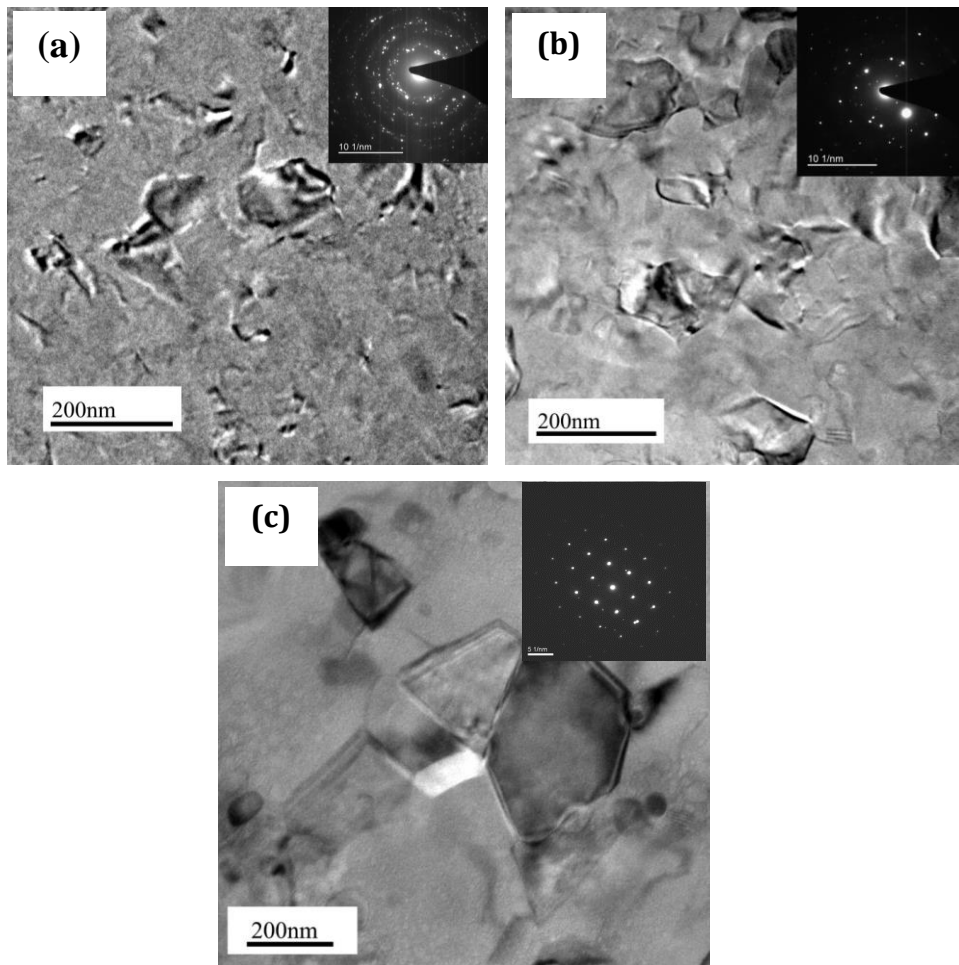


Fig. 5 TEM bright field images of 5r-HPT samples in (a) as HPT processed condition, (b) after heating to 210 °C, and (c) after heating to 300 °C. The corresponding selected area diffraction patterns are at the top-right corner.

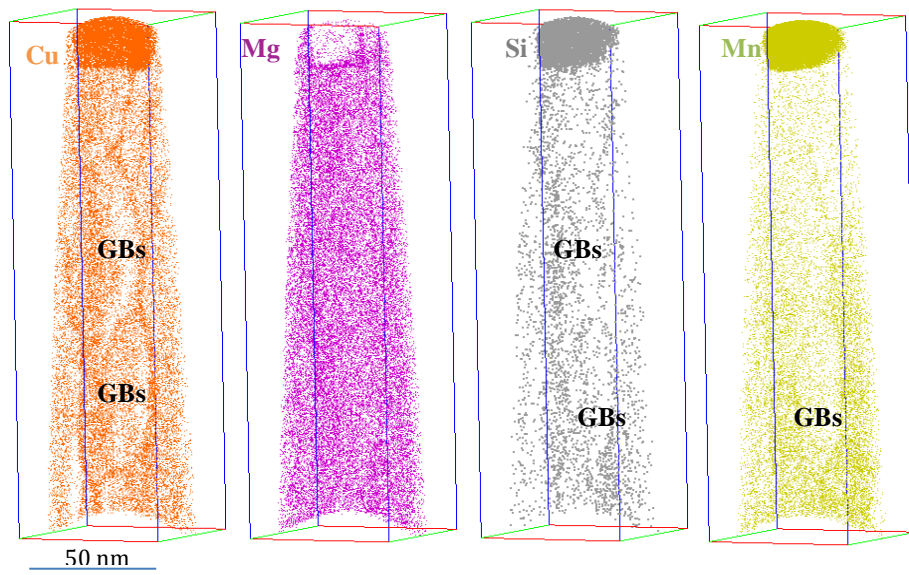


Fig. 6 Mg, Cu, Si and Mn atom maps of 5r-HPT sample aged at ambient temperature near Mn-rich particles.

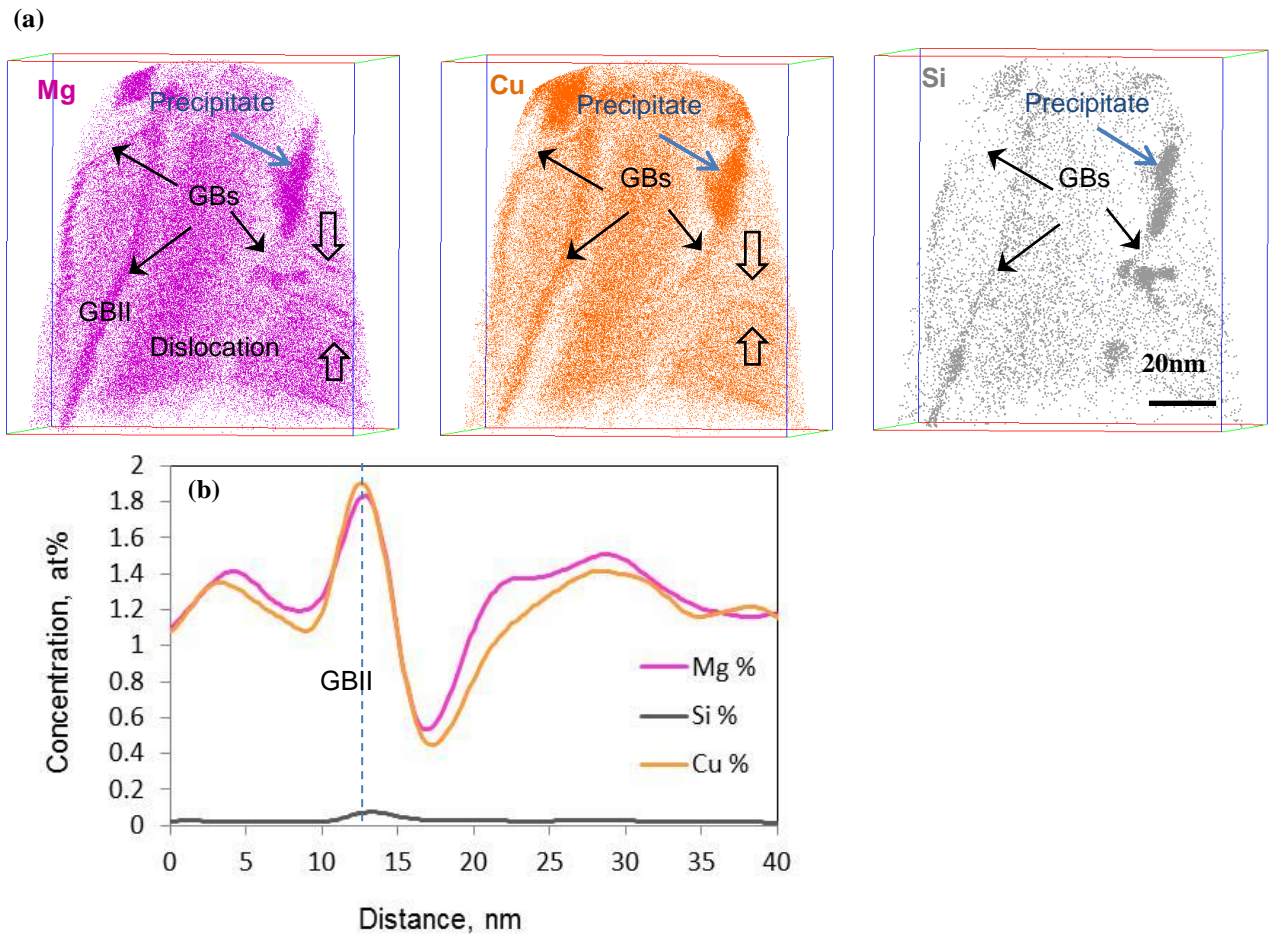


Fig. 7 APM of 5r-HPT sample annealed at 210 °C (a) Mg, Cu and Si atom maps (b) Mg, Cu and Si profiles measured using an analysis box with its z-axis parallel to the plane normal of the grain boundary.

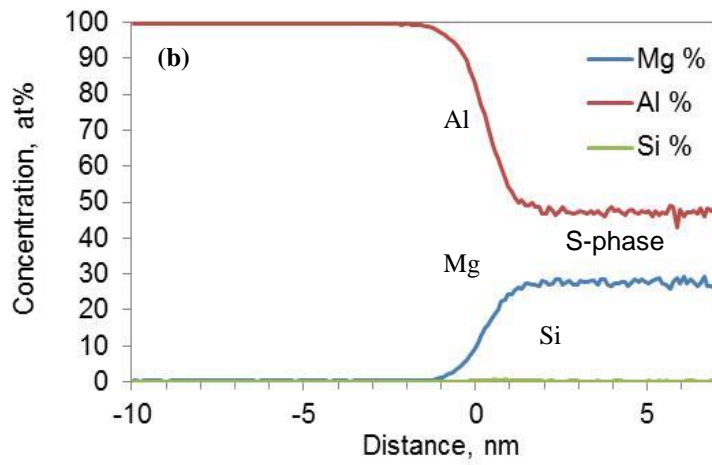
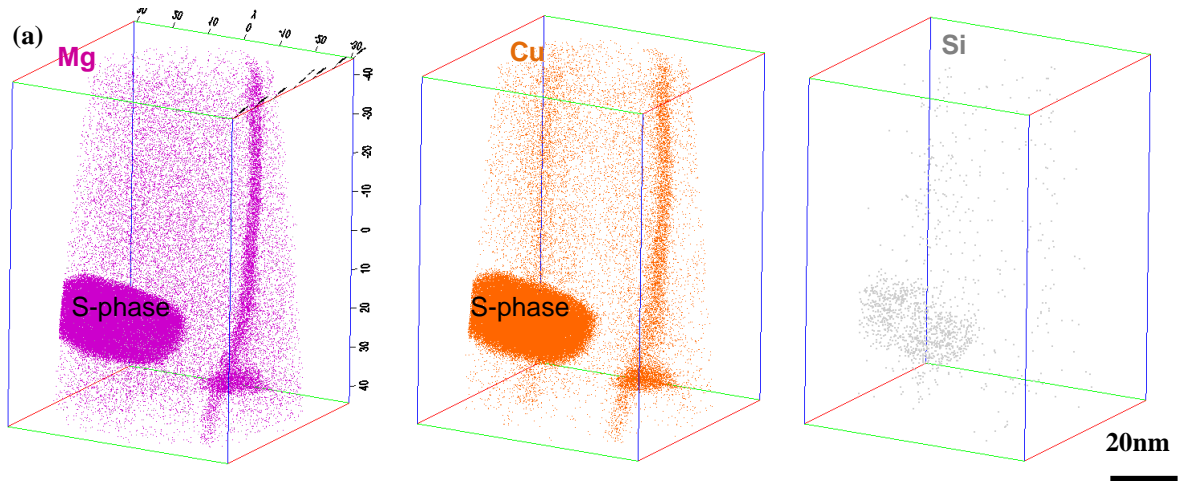


Fig. 8 (a) Mg, Cu and Si atom maps of 5r-HPT sample aged at 300°C (b) concentration profiles of Al, Mg, and Si across the precipitates (the balance is Cu).